

A LUMINOUS INFRARED COMPANION IN THE YOUNG TRIPLE SYSTEM WL 20

MICHAEL E. RESSLER^{1,2,3}

Jet Propulsion Laboratory, California Institute of Technology, 4800 Oak Grove Drive, Pasadena, CA 91109

AND

MARY BARSONY³

Space Science Institute, Suite A353, 3100 Marine Street, Boulder, CO 80303-1058

Received 2000 August 11; accepted 2000 November 7

ABSTRACT

We present spatially resolved near- and mid-infrared (1–25 μm) imaging of the WL 20 triple system in the nearby ($d = 125$ pc) ρ Ophiuchi star-forming cloud core. We find WL 20 to be a new addition to the rare class of “infrared companion systems,” with WL 20 E and WL 20 W displaying Class II (T Tauri star) spectral energy distributions (SEDs) and total luminosities of 0.61 and 0.39 L_{\odot} , respectively, and WL 20 S, the infrared companion, having a Class I (embedded protostellar) SED and a luminosity of 1.0–1.8 L_{\odot} . WL 20 S is found to be highly variable over timescales of years, to be extended (40 AU diameter) at mid-IR wavelengths, and to be the source of the centimeter emission in the system. The photospheric luminosities of 0.53 L_{\odot} for WL 20 E and 0.35 L_{\odot} for WL 20 W estimated from our data, combined with existing, spatially resolved near-IR spectroscopy, allow us to compare and test current pre-main-sequence evolutionary tracks. The most plausible, nonaccreting tracks describing this system are those of D’Antona & Mazzitelli published in 1998. These tracks give an age of $(2\text{--}2.5) \times 10^6$ yr and masses of 0.62–0.68 M_{\odot} for WL 20 E and 0.51–0.55 M_{\odot} for WL 20 W. The age and mass of WL 20 S cannot be well determined from the currently available data. WL 20 E and W fall into the region of the H-R diagram in which sources may appear up to twice as old as they actually are using nonaccreting tracks, a fact that may reconcile the coexistence of two T Tauri stars with an embedded protostar in a triple system. The derived masses and observed projected separations of the components of the WL 20 triple system indicate that it is in an unstable dynamical configuration, and it may therefore provide an example of dynamical evolution during the pre-main-sequence phase.

Key words: binaries: close — stars: formation — stars: individual (WL 20) — stars: pre-main-sequence

1. INTRODUCTION

The optically undetectable source WL 20 (also known as BKLT J162715–243843 and GY 240; see Barsony et al. 1997 for other aliases) was discovered in a near-infrared bolometer survey of a $10' \times 10'$ region of self-absorbed ^{13}CO emission in the ρ Ophiuchi star-forming cloud (Wilking & Lada 1983). Soon thereafter, WL 20 was detected at 10 μm from ground-based observations (Lada & Wilking 1984) and at longer wavelengths in the pointed-observations mode of the satellite *IRAS*, where it is referred to as YLW 11 (Young, Lada, & Wilking 1986).

In the currently accepted classification scheme of young stellar objects (YSOs) devised by Lada (1987), WL 20 was one of the first sources to be identified as a Class I source (Wilking, Lada, & Young 1989). Empirically, Class I sources have broader than blackbody spectral energy distributions (SEDs), with rising 2–10 μm spectral slopes, $a > 0.3$ (where $a = d \log \lambda F_{\lambda} / d \log \lambda$). Theoretically, the SEDs of Class I sources are interpreted to correspond to a remnant infalling dust-and-gas envelope surrounding a

central protostar-plus-disk system (Adams, Lada, & Shu 1987). The more evolved Class II sources, with $-0.3 > a > -1.6$, are pre-main-sequence (PMS) star-plus-disk systems that have dispersed their remnant infall envelopes.

With the advent of near-IR array detectors, WL 20 was soon resolved into a binary system at 2.2 μm using a pixel scale of $0''.85$ (Rieke, Ashok, & Boyle 1989) and first reported to have an east-west separation of $\approx 2''.7$ from observations with a pixel scale of $0''.78$ (Barsony et al. 1989). This separation corresponds to ≈ 340 AU for an adopted distance to the cloud of 125 pc.

We note that some confusion still exists as to the distance to the ρ Oph clouds, primarily because many authors cite the distance to the adjacent Sco-Cen OB association instead. The distance to the Sco-Cen OB association has been determined to be 160 ± 10 pc photometrically (Whittet 1974) and 145 pc astrometrically (de Zeeuw et al. 1999). By contrast, the distance to the ρ Oph cloud itself has been determined to be 125 ± 25 pc from detailed kinematic studies of the cloud gas (de Geus, de Zeeuw, & Lub 1989; de Geus 1992) and, more recently, by a study of *Hipparcos* parallaxes and Tycho $B - V$ colors of stars of classes III and V, which show an abrupt rise in reddening at $d = 120$ pc, as expected for a molecular cloud (Knude & Høg 1998). We therefore adopt a distance of 125 pc to the cloud in this paper.

The first indication that WL 20 is a triple system came from a deep ProtoCAM survey to identify near-IR counterparts of centimeter continuum sources in the ρ Oph cloud core (Strom, Kepner, & Strom 1995). The VLA source iden-

¹ Visiting Astronomer at the W. M. Keck Observatory, which is operated as a scientific partnership among the California Institute of Technology, the University of California, and the National Aeronautics and Space Administration. The Observatory was made possible by the generous financial support of the W. M. Keck Foundation.

² Visiting Astronomer at the Infrared Telescope Facility, which is operated by the University of Hawaii under contract from the National Aeronautics and Space Administration.

³ Observations with the Palomar 5 m telescope were obtained under a collaborative agreement between Palomar Observatory and the Jet Propulsion Laboratory.

tified with WL 20 is known as LFAM 30 and was imaged at 6 cm with an $11'' \times 5''$ beam (Leous et al. 1991). With the sensitive ProtoCAM images acquired at a pixel scale of $0''.20$, a third and weakest $2.2 \mu\text{m}$ component of the system was easily identified and designated “30S” (for the southern component of LFAM 30), whereas the components of the previously known near-IR binary are referred to as “30E” and “30W” by these authors (Strom et al. 1995). With 30E as the positional reference, 30W is quoted at a separation of $3''.3$ at P.A. 269° , and 30S at a separation of $3''.9$ at P.A. 232° .

Near-IR spectra of the two brighter *K* components of the WL 20 triple system, WL 20 E ($K = 10.13$) and WL 20 W ($K = 10.40$), were presented as part of a spectroscopic survey of YSOs with $K < 10.5$ in ρ Oph (Greene & Lada 1996). The near-IR spectra of both WL 20 E and W were found to be consistent with those of other Class II sources, with a K–M spectral type established for WL 20 E and a more precise K7–M0 spectral type determination for WL 20 W, because of the less severe continuum veiling in its spectrum (Greene & Meyer 1995). At their assumed distance of 160 pc, WL 20 E was determined to have a bolometric luminosity $L_{\text{bol}} = 0.4 L_\odot$ through $A_V = 15.4$, whereas WL 20 W was determined to have $L_{\text{bol}} = 1.7 L_\odot$ through $A_V = 18.1$. Continuum veiling in the spectrum of WL 20 E precluded its placement on the H–R diagram, whereas the lesser veiling in the spectrum of WL 20 W allowed a mass estimate of $0.3 M_\odot$ from its location along a 3×10^5 yr PMS isochrone (Greene & Meyer 1995).

A more recent spectroscopic survey of near-IR sources in the ρ Oph core, including many sources as faint as $K \sim 12$, was obtained at higher spectral resolution ($R = 1200$) than the previously published surveys (with $R \leq 1000$), allowing for significantly improved classifications for G through M spectral types (Luhman & Rieke 1999). These authors assigned a K6 spectral type to WL 20 E (GY 240B), with a bolometric luminosity of $0.55 L_\odot$, and an M0 spectral type to WL 20 W (GY 240A) with $L_{\text{bol}} = 1.4 L_\odot$ (they also assumed a distance of 160 pc). Both sources were found to have a foreground extinction of $A_V = 16.3$. WL 20 S, with $K \sim 12.6$, was excluded from this survey as well, because of its relative dimness at near-IR wavelengths.

Interestingly, the discrepancy between the Class I SED classification of WL 20, on the one hand, and its near-IR Class II spectroscopic classifications, on the other, has not been remarked upon previously. This inconsistency can only be addressed by producing spatially resolved SEDs of the individual components of this triple system. Until now, the highest spatial resolution photometry of WL 20 longward of $4.8 \mu\text{m}$ has been through a $6''$ – $8''$ aperture—confusing all three components (Lada & Wilking 1984). In order to better constrain the properties of WL 20 S, and of the triple system of which it is a member, we have obtained new, unprecedentedly high (subarcsecond) spatial resolution, ground-based mid-infrared images of the WL 20 system, at six separate wavelengths spanning the 8– $25 \mu\text{m}$ atmospheric window. In addition, we present spatially resolved near-IR imaging of this triple system. Finally, we have performed careful astrometry, allowing us to identify the source of the centimeter continuum emission.

2. OBSERVATIONS

All mid-IR images were obtained with MIRLIN, JPL’s 128×128 pixel Si:As camera. Diffraction-limited images were obtained on the nights of 1996 April 24 at the Palomar

5 m telescope, 1998 March 13–14 on the 10 m Keck II Telescope, and 2000 June 16 at NASA’s 3 m Infrared Telescope Facility (IRTF). Pixel scales of MIRLIN were $0''.15$ at Palomar, $0''.138$ at Keck II, and $0''.475$ at the IRTF. Observations at Palomar and the IRTF were made with the broadband *N* filter ($\lambda = 10.8 \mu\text{m}$, $\Delta\lambda = 5.7 \mu\text{m}$). For reference, the full-width at half maximum (FWHM) of a diffraction-limited image at *N* band is $0''.47$ at Palomar and $0''.78$ at the IRTF. Observations at the Keck II Telescope were made with narrower filters, with central wavelengths (bandwidths) of $7.9 \mu\text{m}$ ($0.76 \mu\text{m}$), $10.3 \mu\text{m}$ ($1.01 \mu\text{m}$), $12.5 \mu\text{m}$ ($1.16 \mu\text{m}$), $17.9 \mu\text{m}$ ($2.00 \mu\text{m}$), $20.8 \mu\text{m}$ ($1.65 \mu\text{m}$), and $24.5 \mu\text{m}$ ($0.76 \mu\text{m}$); corresponding FWHMs range from $0''.17$ at $7.9 \mu\text{m}$ to $0''.53$ at $24.5 \mu\text{m}$.

The flux of WL 20 at each wavelength was determined by comparison with α Sco at Palomar and at Keck II with a combination of α Boo, α CMa, α CrB, α Hya, β Leo, and σ Sco, the last of which proved to be an easily resolved $0''.45$ binary. The weather at the IRTF was sufficiently poor that no flux standards were observed. Data were obtained with traditional mid-IR chopping and nodding techniques. The raw images were background-subtracted, shifted, and co-added with our in-house IDL routine “MAC” (match and combine). Photometry for the standard stars was performed in $2''.5$ and $2''.3$ diameter apertures for the Palomar and Keck II data, respectively, when the separation between components was adequate (as determined by the intensity contours falling to zero between the sources) and by a combination of aperture summation and point-spread function (PSF) fitting when the separation between WL 20 W and S was not clean. Typically, the flux ratio of a given component with respect to WL 20 E was measured via PSF fitting, and then WL 20 E was calibrated with respect to the standards. The photometric consistency between all the standards at Keck II was found to be 5%–10% at all wavelengths. Though α Sco was the only standard observed at Palomar, multiple observations of it over the course of the night are consistent to 5%, and observations of most other WL sources (Wilking & Lada 1983) observed on that night agree with published values to that level.

Although the IRTF data were taken under extremely nonphotometric conditions, special care was used during the course of the observations to acquire accurate astrometry, in order to establish which of the three components of the WL 20 system is responsible for the observed radio continuum emission (Leous et al. 1991). We imaged three additional nearby Class I radio emitters—LFAM 23 (WL 22), LFAM 27 (WL 15), and LFAM 33 (YLW 15)—in turn with LFAM 30 (WL 20), with as little delay between images as possible, so that registration of the mid-IR source location with respect to the radio coordinates could be made as accurately as possible. If each VLA source were exactly positionally coincident with its respective mid-IR counterpart, then each mid-IR source would fall on exactly the same pixel in each MIRLIN image. In order to reduce our astrometric errors, seven images were obtained of WL 15, five of WL 20, three of WL 22, and two of YLW 15. The resulting scatter in the source positions for WL 22 and YLW 15 was only $0''.5$, allowing relative astrometric determinations to this accuracy.

Near-IR images of WL 20 were acquired with ProtoCAM, a 58×62 InSb array on the IRTF, atop Mauna Kea, on the night of 1990 August 3, at 1.29, 1.67, 2.23, 3.55, and $3.82 \mu\text{m}$. The pixel scale of these observations was $0''.35$. The

data were not photometric: thin cirrus clouds were present throughout the observations. Software aperture photometry ($4''.5$ apertures) was performed on the standards (HD 147889 and BD +65°1637), and the fluxes were found to be consistent only at the 30%–50% level over a fairly wide range of air masses. Nevertheless, even under such conditions, the *intensity ratios* between the components of WL 20 (i.e., the flux ratio of WL 20 W/E and of WL 20 S/E) should be unaffected by weather because the sources all fall within the instantaneous field of view.

3. RESULTS

3.1. Imaging, Photometry, and SEDs

We present diffraction-limited ($\sim 0''.25$ resolution at $10\ \mu\text{m}$) mid-IR images of the WL 20 triple system acquired with MIRLIN at the Keck II Telescope, along with representative shorter wavelength images acquired with PRO-CAM at the IRTF, in Figure 1. We list the source separations and position angles derived from mean positions obtained from the 7.9, 10.3, and $12.5\ \mu\text{m}$ images in

TABLE 1
RELATIVE POSITIONS OF THE THREE COMPONENTS

Pair	Separation (arcsec)	Separation (AU)	Position Angle (deg)
W with respect to E	3.17 ± 0.01	400	270.1 ± 0.3
S with respect to E	3.66 ± 0.03	460	232.2 ± 0.2
S with respect to W	2.26 ± 0.02	280	173.0 ± 0.3

Table 1. The individual components of the WL 20 triple system are labeled in Figure 1e (the $10.3\ \mu\text{m}$ image). It is evident from inspection of Figure 1 that whereas WL 20 S is the weakest source of the system at the shortest wavelengths, it gradually brightens toward the longer wavelengths, just as its companions to the north are dimming. Eventually, WL 20 S dominates the system luminosity at the longest wavelengths (17.9 , 20.8 , and $24.5\ \mu\text{m}$).

We have used a combination of software aperture summation and PSF fitting to obtain photometric information for each component of the WL 20 system individually.

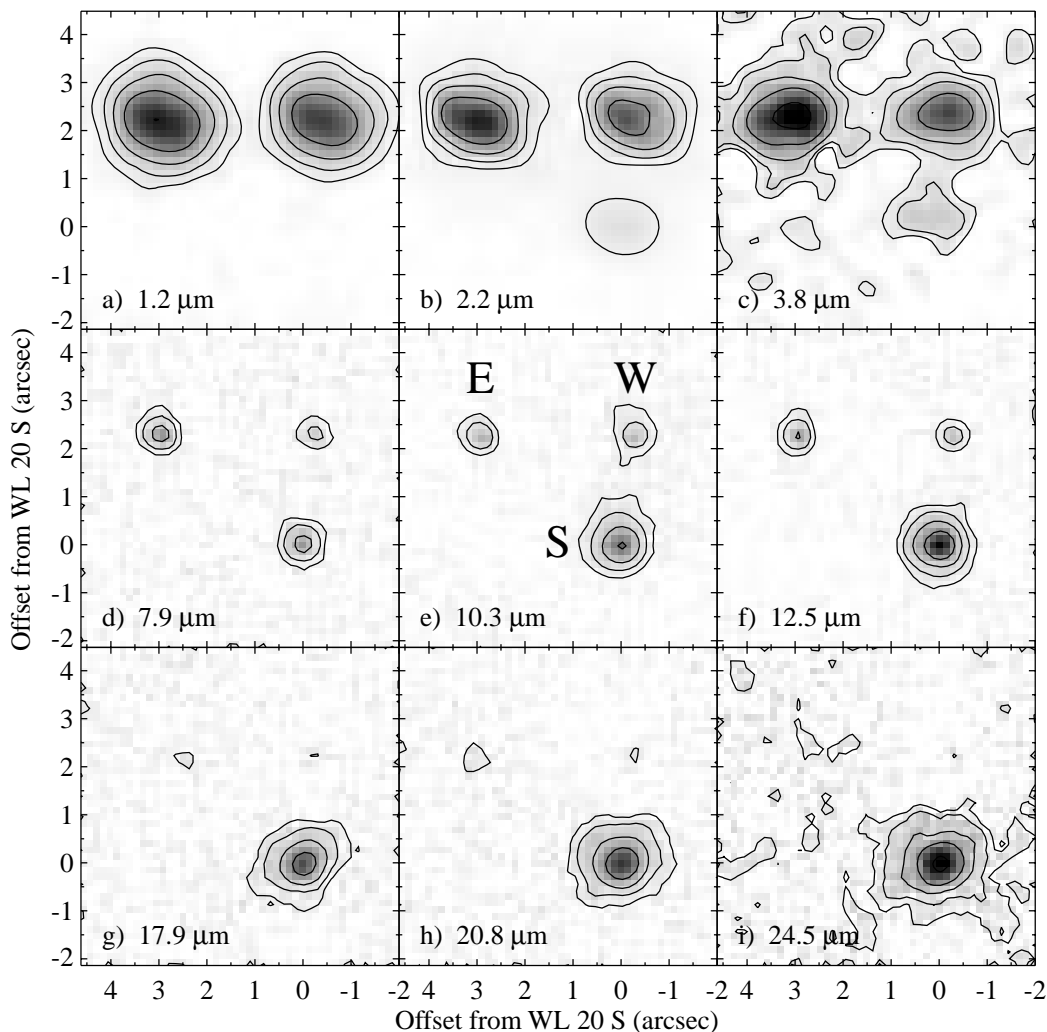


FIG. 1.—Images of the WL 20 triple system at near- and mid-IR wavelengths. (a–c) Images of the WL 20 system acquired with PRO-CAM at the IRTF ($0''.35\ \text{pixel}^{-1}$, resampled to $0''.138\ \text{pixel}^{-1}$); (d–i) MIRLIN Keck II images ($0''.138\ \text{pixel scale}$). Contours in each panel represent the flux density in Jy arcsec^{-2} and are spaced by 1 mag. The lowest contour in (a) is $400\ \mu\text{Jy}$; in (b) it is $4\ \text{mJy}$; in (c)–(f), $40\ \text{mJy}$; and in (g)–(i), $160\ \text{mJy}$. The individual system components, WL 20 E, W, and S, are identified in (e). The field of view of each panel is $6''.6 \times 6''.6$. East is to the left, and north is up for all of the images presented in this paper. Source separations are $3''.17 \pm 0''.01$ between WL 20 E and W and $2''.26 \pm 0''.02$ between WL 20 W and S.

Fluxes derived from the new data presented here, as well as all known previously published values, are listed in Table 2.

The resulting SEDs are presented in Figures 2 and 3. The SEDs for WL 20 E and W (Fig. 2a) are consistent with their being reddened Class II sources with modest excesses at

long wavelengths, in agreement with the near-IR spectroscopic results. The spectral slopes, $a = -0.79$ for WL 20 E, and $a = -0.91$ for WL 20 W, are as expected for Class II sources. In fact, the shape of the SED of WL 20 W is quite close to a reddened blackbody in the near-IR (i.e., a small

TABLE 2
FLUXES FOR THE WL 20 COMPONENTS

WAVELENGTH (μm)	THIS WORK (mJy)			SKS ^a (mJy)			THIS WORK TOTAL (mJy)	SKS TOTAL ^a (mJy)	OTHER TOTAL (mJy)
	E	W	S	E	W	S			
1.29	3.8*	3.0*	0.03*	4.2	3.2	<0.1	6.8*	7.5	6.9 ^b
1.67	32.7*	25.6*	0.79*	30.7	23.3	1.7	59.1*	55.8	50.6 ^b
2.23	87.1*	61.0*	5.9*	57.1	44.6	6.0	154	108	125 ^b
3.55	123.2*	69.7*	15.3*	208*	...	158 ^b
3.82	137.7*	70.3*	18.6*	85.1	49.4	7.1	227*	142	...
4.78	92.6	28.0	7.2	...	128	...
6.7	160, 240, 290 ^c
7.9	121.0	38.4	123.0	282
10.2	180 ^d
10.3	72.6	49.6	345.0	467
10.8	79.0	51.5	281.0	412
11.5	630 ^e
12	1200 ^e
12.5	86.8	44.3	610.0	741
17.9	78.0	93.9	2720.0	2900
20.8	109.0	117.0	3700.0	3930
24.5	<155.0	<155.0	6600.0	6910
25	11200 ^e
60	55600 ^e
850	300 ^f
1300	95 ^g

NOTE.—Values with an asterisk are nonphotometric.

^a Strom et al. 1995.

^b Wilking & Lada 1983.

^c Wilking et al. 2001.

^d Lada & Wilking 1984.

^e Young et al. 1986; data have been color-corrected as described in the text.

^f Ward-Thompson & Kirk 2001.

^g André & Montmerle 1994.

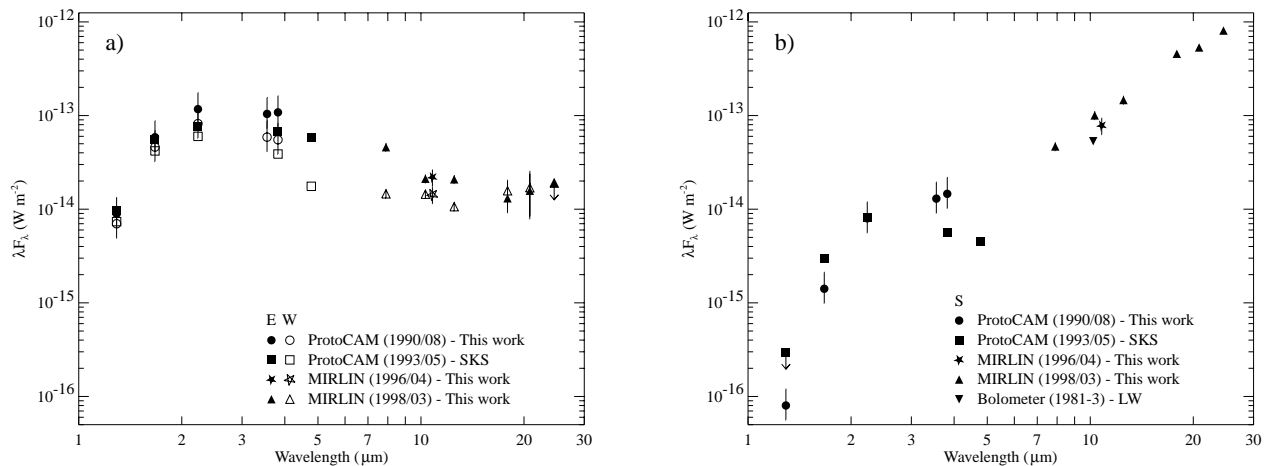


FIG. 2.—Spatially resolved SEDs of the three components of the WL 20 system. (a) Spectral energy distributions of the east and west components of WL 20. Filled symbols represent photometry for WL 20 E, and open symbols show photometry for WL 20 W. Squares are ProtoCAM data from Strom, Kepner, & Strom (1995), circles are ProtoCAM data from 1990 August, stars indicate our N -band MIRLIN photometry from 1996 April Palomar 5 m observations, and triangles indicate mid-IR MIRLIN photometry from 1998 March Keck II observations. The negative 2–10 μm spectral slopes characteristic of Class II objects are evident for each of these two sources. (b) Spectral energy distribution of WL 20 S plotted on the same scale as (a). Symbols are as in (a), except that filled symbols now represent WL 20 S and the total N -band system flux from Lada & Wilking (1984) has been added (*downward-pointing triangle*). The SED of WL 20 S is of a completely different character from that of either WL 20 E or W and is similar to that of younger Class I sources.

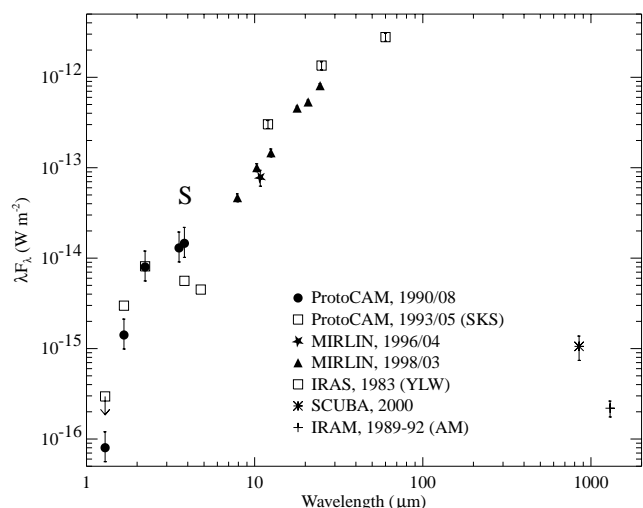


FIG. 3.—The SED of WL 20 S from 1 μm to 1.3 mm: the full spectral energy distribution of the southern component of WL 20 including *IRAS*, SCUBA, and millimeter data. (There is no *IRAS* 100 μm point because of the severe confusion in this region.)

near-IR excess, though the excess at mid-IR wavelengths is substantially larger). Thus it is possible that the circumstellar material around WL 20 W may be optically thin enough for silicate emission to be present. Comparison of the 10.3 μm fluxes (near the center of the silicate feature) with the “continuum” fluxes at 7.9 and 12.5 μm suggests a factor of ~ 2 excess at 10.3 μm in WL 20 W with respect to that anticipated from the shape of WL 20 E’s SED. Our single data point is not sufficiently compelling (though it is robust) to warrant a large discussion of silicate emission here, but future spatially resolved mid-IR spectroscopy should address in fine detail the nature of the dust emission and absorption in these Class II sources.

The SED of WL 20 S (Fig. 2b), however, is that of a Class I source, with $a = +1.44$. Given that there is a generally continuous slope between our ground-based mid-IR data for WL 20 S and the far-infrared and millimeter fluxes for the entire WL 20 system, we have attributed all the longer wavelength flux observed in this system to WL 20 S (Fig. 3). For the case of the millimeter emission, this assumption may be tested by future interferometric observations.

We color-correct the *IRAS* fluxes for this source in order to make the best luminosity estimate possible. We use our narrowband observations with MIRLIN at 12.5 and 24.5 μm along with others’ 850 μm and 1.3 mm observations to constrain the shape of the far-IR SED so that the color correction terms may be estimated. The spectral slope implied by all the narrowband mid-IR data follows a $F_\nu \propto \nu^{-3}$ power law over this range, so we deredden the 12 and 25 μm fluxes according to that rule from the *IRAS* Explanatory Supplement (Beichman et al. 1988), dividing them by factors of 0.91 and 0.89, respectively. The SED clearly peaks in the vicinity of 60 μm (or at least does not rise significantly throughout the entire 45–80 μm passband). We therefore fitted the 60, 850, and 1300 μm data with a ~ 80 K graybody. In fact, the 60 μm color correction at this temperature is quite small (divide by 0.97) and is not very sensitive to modest excursions in temperature (60–120 K), so even using the uncorrected flux would be adequate. The resulting data show the usual factor of 2–3 excess of the *IRAS* measured

flux versus the ground-based data (see, e.g., Lada & Wilking 1984).

3.2. Luminosities of the Individual Components of WL 20

We compute the luminosity of each Class II component of the WL 20 system (E and W) by integrating under the curves displayed in Figure 4. The data points from 1.2 to 18 μm have been dereddened using a Draine & Lee (1984) extinction curve assuming $A_V = 16.3$ (Luhman & Rieke 1999). Though we assume $A_V = 16.3$, we can rule out $A_V > 18$ from our data since the near-IR data then have a slope steeper than a blackbody, and $A_V < 15$ can be ruled out as the near-IR data would then be too red to be consistent with the flux from a ~ 4000 K photosphere. We use a power-law extrapolation from 18 through 1300 μm consistent with the spectral slope from 3 to 18 μm ($F_\nu \propto \nu^{0.45}$) to estimate the source fluxes at far-IR through millimeter wavelengths. Other extrapolations for the fluxes from 18 μm to longer wavelengths may be used (e.g., no flux at all past 18 μm , or even a constant flux between 18 and 1300 μm), but none change the estimated luminosity more than 2%, since the majority of the energy is emitted at shorter wavelengths.

A strict lower limit to the source luminosities, the “infrared” luminosities, is arrived at by integrating under the dereddened 1–18 μm data points and the long-wavelength extrapolation described above using simple trapezoidal integration. We find an infrared luminosity of $0.26 L_\odot$ for WL 20 E, and $0.17 L_\odot$ for WL 20 W. We have used our near-IR photometry to compute the luminosity rather than that of Strom et al. (1995) since this provides

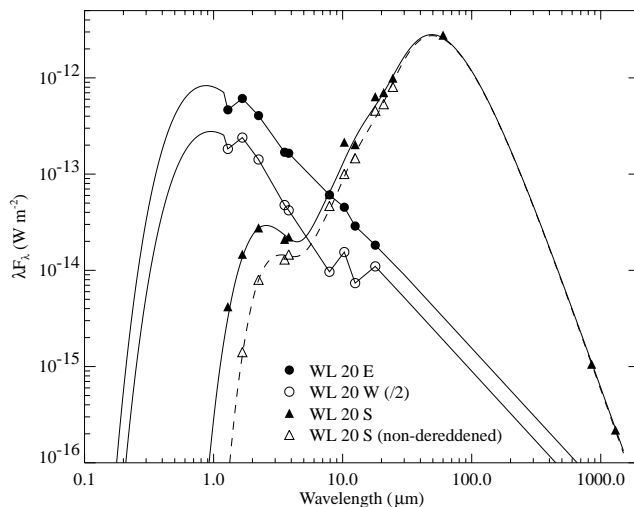


FIG. 4.—Luminosity determinations for the three components of the WL 20 system. The data for the three components, along with the curves used to obtain the best luminosity estimates, are plotted. The data for WL 20 W have been divided by 2 for clarity. The data for all three components have been dereddened by assuming a $A_V = 16.3$ foreground screen and a Draine & Lee (1984) extinction curve (solid lines). A non-dereddened curve for WL 20 S (dashed line) is also plotted for the case in which all the extinction is local to the source and dereddening is not appropriate. The “model” curves for WL 20 E and W are represented directly by the data from 1 to 18 μm , a blackbody of the appropriate effective temperature (see text) from 0.1 to 1.2 μm , and a power law beyond 18 μm . The curves for WL 20 S are composites of several blackbodies modified for extinction and dust emissivity. The curves for WL 20 S assume that all far-IR and millimeter flux originates from WL 20 S; in the case that only 50% does (see text), the 60 μm and millimeter points are reduced by a factor of 2 and the model curves above 40 μm are correspondingly reduced.

better continuity with the mid-IR data. However, use of the Strom et al. near-IR data reduces our luminosity estimates by only $0.03 L_{\odot}$ for each component.

To obtain a more accurate value of the total luminosity of each component, however, we scale a blackbody spectrum from 0.1 to $1.2 \mu\text{m}$ at the effective temperatures found by Luhman & Rieke (1999) to match the observed infrared data values. Luhman & Rieke (1999) found temperatures of 4205 K for WL 20 E and 3850 K for WL 20 W. We then integrate under this blackbody curve in addition to the infrared data points (Fig. 4, *solid lines*). This technique yields total luminosities of $0.61 L_{\odot}$ for WL 20 E and $0.39 L_{\odot}$ for WL 20 W. Integration of only the blackbody (over all wavelengths), which should approximate the emission of the photosphere without luminosity from the disk, yields 0.53 and $0.35 L_{\odot}$, respectively. These values are appropriate for comparison with the PMS evolutionary models discussed in § 4.2.

For WL 20 S, computing the luminosity is complicated by two issues: if and how to deredden the data, and how to partition the flux at far-IR and millimeter wavelengths, where the sources are not resolved. With regard to dereddening, since no photospheric measurements are available we can assume either that all the extinction is local and most of the near-IR photons are absorbed and reradiated in the far-IR, where the extinction is much smaller, or that the same $A_V = 16.3$ foreground screen is present as for the other two components (and there is a correspondingly lower local extinction). Dereddening the data in the first case would “double count” the near-IR photons, while dereddening in the second is the correct procedure. However, since most of the energy is radiated in the mid-IR through millimeter regime, where the extinction is small, the final luminosity estimate changes only 10% after dereddening.

As for the far-IR and millimeter fluxes, we can establish an upper bound on the luminosity by assuming that all the $60 \mu\text{m}$ *IRAS* flux from Young et al. (1986), the $850 \mu\text{m}$ flux from SCUBA (Ward-Thompson & Kirk 2001), and the 1.3 mm measurement from André & Montmerle (1994) originate from WL 20 S. As a lower bound, we assume that 50% of the flux originates from WL 20 S; this is consistent with the ground-based 12 and $25 \mu\text{m}$ points’ being roughly half the *IRAS* points. In either case, this necessarily implies that most of the dust in the WL 20 system surrounds WL 20 S. Also, the *IRAS* data presumably contain some contaminating flux from the nearby source WL 19; however, we know that WL 19 is quite faint with respect to WL 20 at $10.8 \mu\text{m}$ (a factor of 5.6 fainter; Barsony, Ressler, & Casement 2001); therefore, its effect on our luminosity estimate will be very small.

With all the above factors in mind, a simple trapezoidal integration of the WL 20 S fluxes yield a bolometric luminosity of $1.28 L_{\odot}$ if all the extinction is local, and $1.40 L_{\odot}$ if the data points are first dereddened for an $A_V = 16.3$ foreground screen. In both these instances, all the observed far-IR and millimeter fluxes were assigned to WL 20 S. If, instead, we assign only half the observed far-IR and millimeter flux to WL 20 S, the corresponding values for the luminosity become 0.84 and $0.95 L_{\odot}$, respectively. Use of the Strom et al. (1995) near-IR data, instead of our near-IR data, increases these values by only $0.04 L_{\odot}$.

To improve the above luminosity estimates for WL 20 S, given the coarseness of the trapezoidal integration algo-

rithm and the sparseness of the data between 25 and $850 \mu\text{m}$, where the SED peaks, we have constructed a smooth model curve that passes through all of the data points under which to integrate. This curve is constructed by assuming a $T_{\text{eff}} = 4000 \text{ K}$ photosphere, two blackbodies at $T = 300 \text{ K}$ and $T = 150 \text{ K}$ to represent the disk emission, and a modified $T = 65 \text{ K}$ blackbody dust envelope with a λ^{-1} emissivity law. This model was created only to obtain a smooth curve that represents the SED of WL 20 S adequately for integration; it is not intended to be a physical description of the object. The corresponding derived luminosities for WL 20 S then become $1.71 L_{\odot}$ for the curve passing through the data points, $1.82 L_{\odot}$ for the curve dereddened by $A_V = 16.3$, assuming all of the far-IR and millimeter flux to originate from WL 20 S, and 1.04 and $1.14 L_{\odot}$, respectively, for the case in which only half the observed far-IR and millimeter fluxes are attributed to WL 20 S. Therefore, the true luminosity of WL 20 S lies somewhere between 1.0 and $1.8 L_{\odot}$, making this source the most luminous member of the system by a factor of ~ 2 .

3.3. Variability of the Class I Source, WL 20 S

The slight discrepancy of the measured flux in the broadband N ($10.8 \mu\text{m}$) filter for WL 20 S in the 1996 April Palomar data with respect to the flux measured for this source with the $10.3 \mu\text{m}$ silicate filter in the 1998 March Keck II data led us to examine the relative photometry of the components of the WL 20 system as a function of time (see Table 2). For this purpose, we replot the spatially resolved fluxes as intensity ratios with respect to the fluxes of component WL 20 E in Figure 5. The squares in this figure represent the previously published photometry from Strom et al. (1995) for data acquired in 1993 May. The circles represent the relative photometry from our 1990 August ProtoCAM observations. (Because these are now relative

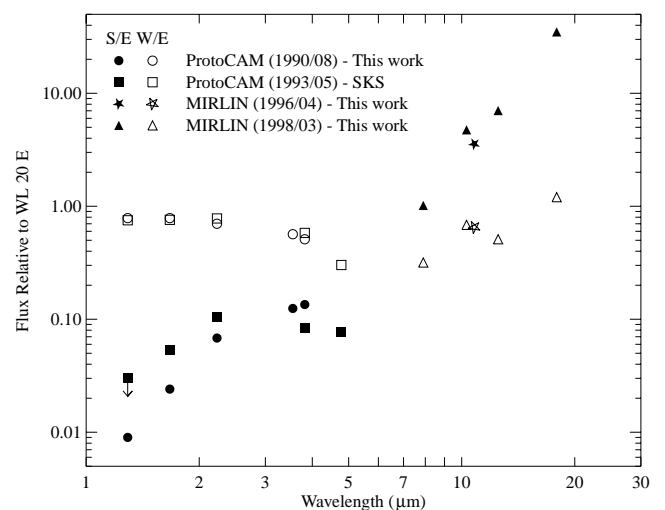


FIG. 5.—SED variability of WL 20 S. Open symbols represent the ratio of the flux from WL 20 W with respect to WL 20 E; filled symbols represent the ratio of the flux from WL 20 S with respect to WL 20 E; otherwise, the symbols are the same as in Fig. 2a. There was a significant shift in the spectral shape of the Class I source, WL 20 S, between the 1990 and 1993 ProtoCAM observations (*filled circles vs. filled squares*), while the fluxes and spectral shape of the Class II source, WL 20 W, over this wavelength range remained essentially constant (*open circles and squares*). The change in the WL 20 S/E flux ratio at $10 \mu\text{m}$ is also significant between the 1996 and 1998 MIRLIN observations.

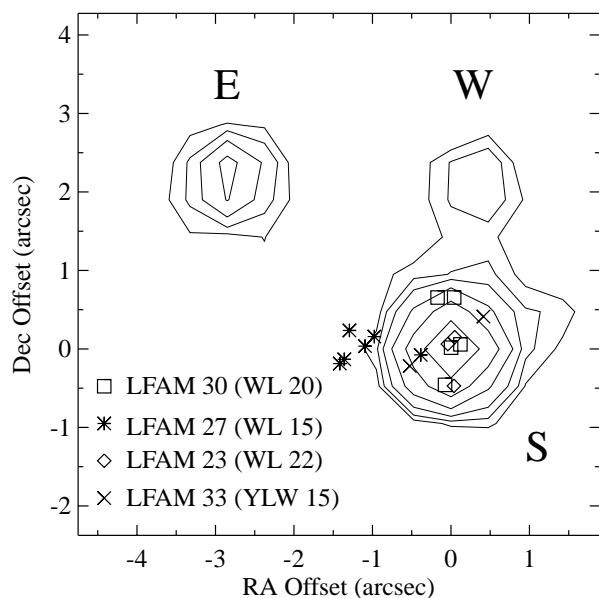


FIG. 6.—Identification of LFAM 30 with WL 20 S: a plot of the offset positional errors between LFAM 30 and WL 20 derived by successive offsetting between the centimeter and mid-IR positions of four Class I radio emitters, indicated in the symbol key, superposed on the $10.3\ \mu\text{m}$ contour plot of the WL 20 system. If we assume that LFAM 23 and LFAM 33 are exactly coincident with their mid-IR counterparts, WL 22 and YLW 15, then LFAM 30 is coincident with WL 20 S. The scatter in the relative positions is $0''.5$. WL 15 appears to be offset from the published radio position by about $1''$ in right ascension, but this is consistent with the coarseness of the published VLA position ($0''.1$ in R.A.). Even with this uncertainty, WL 20 E and W are ruled out as possible counterparts to the VLA source.

ratios, the variations in the sky should divide out, and we believe the relative photometric errors are less than 5%.) The different epochs of MIRLIN observations are represented by stars and triangles. From this plot it can be seen that whereas WL 20 W does not vary significantly over this wavelength range and timescale, WL 20 S varies greatly (factor of ~ 3) in the near-IR and perhaps even changes the shape of its SED over the timescale of a few years.

Even at $10\ \mu\text{m}$, the variations appear to be significant. Though our MIRLIN results show only a 25% increase between 1996 and 1998, Lada & Wilking (1984) report a flux of 180 mJy for the *entire system* (all three components should have been contained in their $6''$ beam), whereas our total system flux from 1998 is 470 mJy. If we assume WL 20 E and W to be constant over this entire timespan, WL 20 S would have had a flux of only 60 mJy in 1981–1983, resulting in a nearly sixfold increase in 15 years.

Wilking et al. (2001) have also reported that WL 20 brightened from 160 to 290 mJy at $6.7\ \mu\text{m}$ from 1996 through 1998. Piecing the observations together as well as

possible, it seems that WL 20 S was in a low-luminosity state in the early 1980s, brightened until ~ 1990 , faded during the early 1990s, and has been increasing since the mid-1990s. Given the changing shape of the SED, it may be that as the accretion rate increases, both the luminosity and the local extinction rise, leading to large increases in the mid- and far-IR and perhaps a decline in the near-IR. Though many more temporal data are required to put these speculations on a firm footing, they seem plausible with the data in hand. We conclude that much of the total luminosity of WL 20 S is derived from accretion, and that the stellar luminosity cannot be directly determined from our data.

3.4. Astrometry and the Identification of LFAM 30 with WL 20 S

In their VLA survey of the ρ Oph cloud, Leous et al. (1991) found that a number of cluster members were radio emitters. One of their radio sources, LFAM 30, was associated with WL 20. However, until now it had not been possible to identify which of the three components of the WL 20 system is responsible for the radio emission. In order to solve this problem, we obtained the astrometric data at the IRTF as described in § 2. Assuming the mean position of LFAM 23 (WL 22) to be the zero point, we plot the offsets from the Leous et al. radio positions of these sources superposed upon the N -filter image of WL 20 in Figure 6. We find that, to within $\pm 0''.5$, LFAM 30 is coincident with WL 20 S.

WL 15 appears to be offset $1''$ east from the radio position. This is almost certainly due to the fact that the VLA coordinates were published only to the nearest $0''.1$, which is $1''.4$ on the sky at the declination of WL 20, so an offset of $1''$ is not unexpected. However, even if the total error were due to purely random pointing errors (which is unlikely given the small scatter for the other objects), the consistency of the radio offsets is sufficiently good that a correspondence between LFAM 30 and either WL 20 E or W is ruled out.

3.5. Extended Mid-IR Structure of WL 20 S

During the course of obtaining PSF-fitted fluxes for each component of the WL 20 system, we discovered that WL 20 S is extended at all mid-IR wavelengths. In order to demonstrate this, we present images of the source after the subtraction of a scaled (to the peak intensity value) PSF, as well as intensity crosscuts along an east-west axis at 12.5 , 17.9 , 20.8 , and $24.5\ \mu\text{m}$ in Figures 7 and 8. Also shown for comparison are similarly obtained intensity crosscuts of the flux standards used for the observations at each wavelength. Whereas the flux standards are unresolved point sources, as are the two Class II sources, WL 20 E and W, WL 20 S is seen to have a definite extent above that expected for a point source at each of the four plotted wavelengths. Some-

TABLE 3
SOURCE SIZE OF WL 20 S

Wavelength (μm)	WL 20 S FWHM (arcsec)	PSF FWHM (arcsec)	rms Difference (arcsec)	Diameter (AU)
12.5.....	0.45	0.28	0.36	45
17.9.....	0.53	0.38	0.37	46
20.8.....	0.58	0.43	0.38	48
24.5.....	0.60	0.51	0.32	40

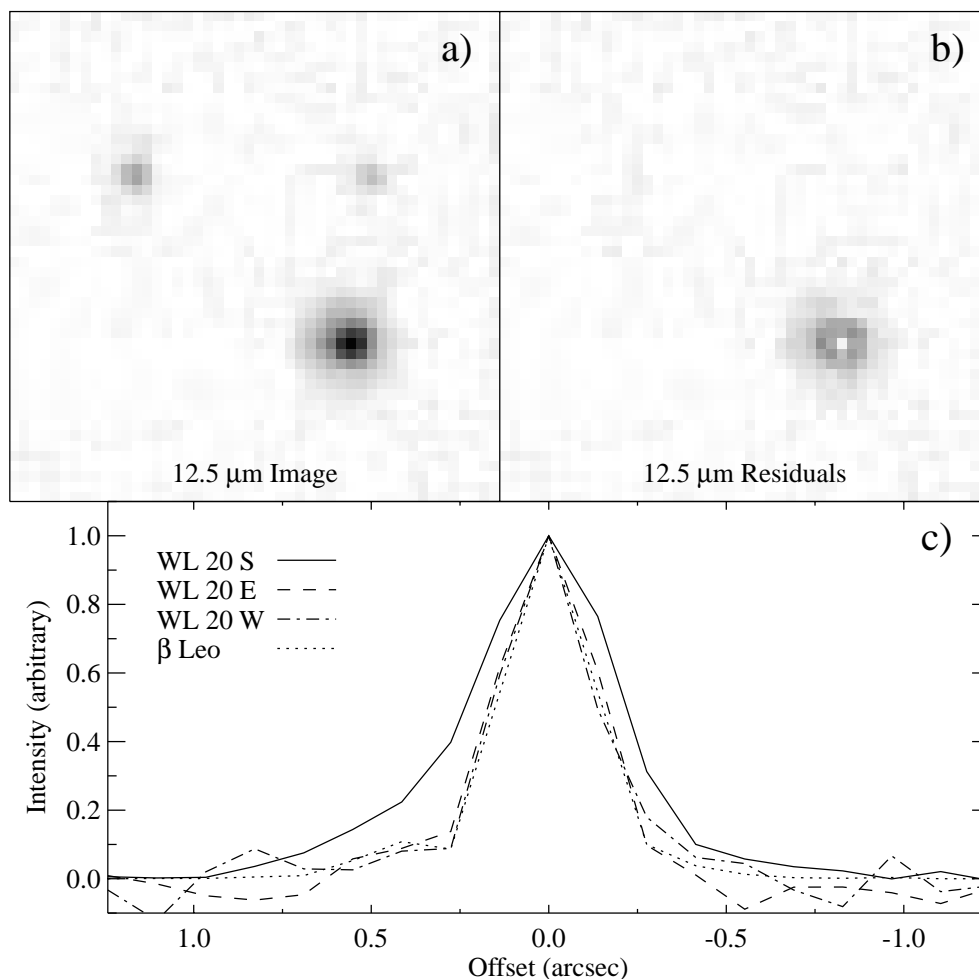


FIG. 7.—The $12.5 \mu\text{m}$ extent of WL 20 S. (a) Gray-scale image of the WL 20 system at $12.5 \mu\text{m}$ at a plate scale of $0''.138 \text{ pixel}^{-1}$ ($6''.6 \times 6''.6$ field of view). (b) Leftover emission after subtraction of appropriately scaled (to the peak flux value) images of β Leo, a point source, placed at the positions of WL 20 E, W, and S. Scaled PSFs can completely account for all of the $12.5 \mu\text{m}$ emission from WL 20 E and W, as demonstrated by the lack of residual flux emission seen at their positions. This same panel demonstrates clear evidence for extended $12.5 \mu\text{m}$ flux associated with WL 20 S after point-source subtraction. (c) East-west cuts across the point-source calibrator, β Leo, and WL 20 E, W, and S. Only WL 20 S has a broadened core and wings, indicative of emission more extended than a point source.

what surprisingly, the physical size of the emitting region is fairly constant at all four wavelengths (Table 3). The rms diameter (observed FWHM minus PSF FWHM) is about $0''.36 \pm 0''.03$, or 45 ± 3 AU at the distance of WL 20. The source size does not increase significantly with increasing wavelength, as is common in many Class I YSOs.

4. DISCUSSION

4.1. WL 20: An “Infrared Companion” System

Infrared companion systems are young binary or multiple systems in which one of the members is significantly “redder” than the other members of the system. “Red” in this context means that the companion is often very faint or invisible at optical and, perhaps, even the shorter near-IR wavelengths but very often dominates the luminosity of the system in the near- and mid-IR. A prototypical example of such a system is T Tau, with a projected separation of $0''.73$, corresponding to ~ 100 AU at the source. The northern component, T Tau N, exhibits a typical Class II spectrum. Although the SED of its companion, T Tau S, is much redder than that of a typical T Tauri star, suggesting local-

ized, high extinction toward this source, the SED nevertheless peaks in the near-IR (i.e., at $\sim 5 \mu\text{m}$), unlike a Class I SED, which peaks toward the far-IR. T Tau S is detected only at wavelengths $\geq 2.2 \mu\text{m}$, although its bolometric luminosity exceeds that of T Tau N by a factor of 2. Furthermore, T Tau S has been shown to be variable (at the level of 2 mag flux increases in the infrared) over a 5 yr time interval (Ghez et al. 1991; Gorham et al. 1992). Large near-IR variability is a characteristic trait of infrared companion systems (Mathieu 1994).

From our spatially resolved SEDs of the individual components of the WL 20 triple system, we can confidently assert WL 20 to be a newly identified member of the class of infrared companion systems. Table 4 lists the properties of each individual source derived from this work, with the spectral types and effective temperatures for WL 20 E and W from Luhman & Rieke (1999).

The possibilities usually cited to explain such “infrared companion” systems include the following:

1. *A chance superposition of sources.*—It may be that WL 20 S is not physically associated with WL 20 E and W; it is

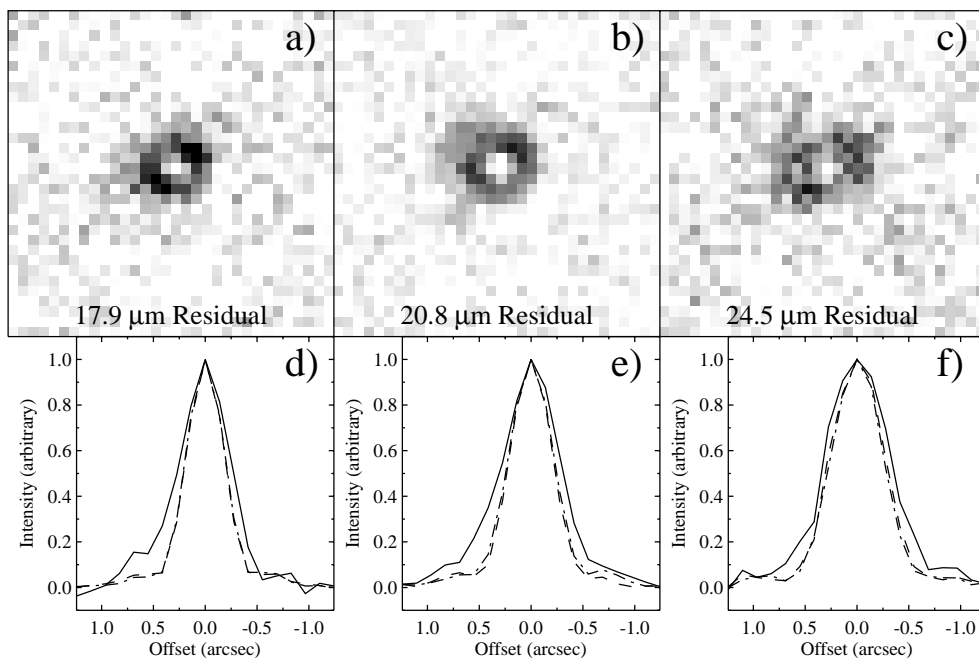


FIG. 8.—The 17.9, 20.8, and 24.5 μm extent of WL 20 S. (a–c) Result of subtracting a scaled PSF from the images at 17.9, 20.8, and 24.5 μm , respectively, covering a $4''.4 \times 4''.4$ field of view. Excess, extended emission is plainly visible at each wavelength and is perhaps elongated in a southeast-to-northwest orientation. (d–f) East-west intensity crosscuts through WL 20 S (solid line) and two PSF calibrators (α CMa, dashed line; α Hya, dot-dashed line). In all cases, the extended source size of WL 20 S appears to be a constant 45 ± 3 AU, rather than a varying source size that increases with increasing wavelength.

a chance superposition, and therefore WL 20 S can be in any evolutionary state relative to WL 20 E and W. We must stress that we cannot rule out this possibility based on currently available data. It is nevertheless well established that all three sources of the WL 20 system are YSOs, and therefore, all are associated with the ρ Oph cloud. The space density of embedded objects in this cloud ($< 200 \text{ deg}^{-2}$; Kenyon, Lada, & Barsony 1998) is low enough that finding three YSOs apparently separated by such small distances is very unlikely unless they are physically associated. Milli-arcsecond astrometry in the near-IR over a sufficiently long time interval could prove association definitively, either by showing the sources to have a common space motion or a definite orbital motion.

2. *A non-coplanar system in which the infrared companion is viewed “edge-on.”*—It has recently been shown that a Class II source whose flared disk, with its surface heated by the stellar radiation field, could mimic the SED of a Class I source if the disk was in a nearly edge-on orientation to our line of sight (Chiang & Goldreich 1999). Indeed, we argue below that WL 20 S probably does have a flared disk, though the inclination is $\sim 20^\circ$ from edge-on. However, WL

20 S exhibits two phenomena common to infrared companion systems that orientation effects cannot explain if it is simply another Class II object: at 1.0 – $1.8 L_\odot$, it is the dominant luminosity source in the system by a factor of 2, and it is highly variable at both near- and mid-IR wavelengths. Neither of these would be expected if it were simply an extinguished sibling of the other two sources. We therefore consider this scenario unlikely.

3. *A younger age for the infrared companion.*—It may be that WL 20 S formed significantly later than its companions, WL 20 E and W. The projected separations between the components of the WL 20 system range from 280 to 460 AU (see Table 1). These separations correspond to sound-crossing times of order $\sim (1-2) \times 10^4$ yr. Given that typical free-fall times of precollapse cores are of order 10^5 yr, the WL 20 system must have collapsed from a single cloud core. Based on this simple dynamical argument, it is highly unlikely that the individual components of the WL 20 system formed at different times.

4. *Coeval objects in a physical configuration and a certain phase of evolution in which most of the dust accretion is occurring on one of the objects, rather than all three.*—This is

TABLE 4
WL 20 SOURCE PROPERTIES

Source	R.A. (J2000.0) ^a	Decl. (J2000.0)	Sp. Index a	IR Luminosity (L_\odot)	Total Luminosity (L_\odot)	T_{eff} (K)	Type
WL 20 E	16 27 15.82	−24 38 43.4	−0.79	0.26	0.61	4205	K6 Class II
WL 20 W	16 27 15.63	−24 38 43.4	−0.91	0.17	0.39	3850	M0 Class II
WL 20 S	16 27 15.65	−24 38 45.6	+1.44	0.84–1.40	1.04–1.82	...	Class I

NOTE.—Units of right ascension are hours, minutes, and seconds, and units of declination are degrees, arcminutes, and arcseconds.

^a Assumes the right ascension of LFAM 23 is precisely $16^{\text{h}}23^{\text{m}}57^{\text{s}}.50$ (B1950.0).

the most plausible possibility for explaining the properties of the infrared companion, WL 20 S, in the WL 20 system. Indications are that the observed 1.3 mm flux from the WL 20 system is centered on the centimeter source (André & Montmerle 1994), which we have shown is associated with WL 20 S (see Fig. 6). The observed 1.3 mm flux of 95 mJy (André & Montmerle 1994) translates to a circumstellar mass of 0.03 (0.06) M_{\odot} , assuming optically thin emission from dust at temperatures $T_d = 30$ (50) K and $\kappa_{1.3 \text{ mm}} = 0.01 \text{ cm}^2 \text{ g}^{-1}$. Infrared variability, such as observed in WL 20 S (see Fig. 5), signals the presence of active accretion (see, e.g., Beck et al. 2000). The combined picture of this system is reminiscent of recent binary formation models (e.g., Bate & Bonnell 1997) in which one component can be bright and actively accreting relative to a less luminous secondary component, depending on the initial distribution of specific angular momentum in the collapsing protostellar envelope relative to the orbital angular momentum of the system. We consider such a scenario to be the most likely to explain the properties of the WL 20 triple system.

4.2. Testing PMS Tracks with the WL 20 System

To date, only a handful of PMS binary or multiple systems have both spatially resolved spectroscopy and spatially resolved photometry over a wavelength range as broad as presented here (1–25 μm). With these data, we have been able to independently infer the luminosities of WL 20 E and W to significantly higher accuracy (approximately a few percent, apart from systematic effects discussed below) than has been possible previously (see Table 4). This coeval system, with well-determined photospheric luminosities (§ 3.2) and effective temperatures, provides a stringent test to distinguish between currently available PMS evolutionary models. Figures 9a–9d show isochrones (*solid lines*) and isomass evolutionary tracks (*dashed lines*) at the same scale for four different sets of PMS models—Baraffe et al. (1998), D’Antona & Mazzitelli (1998),⁴ Palla & Stahler (1999), and Siess, Dufour, & Forestini (2000), respectively. In each figure, the square denotes WL 20 E and the diamond denotes WL 20 W. Figure 9e shows the range of parameter space over which PMS tracks are customarily plotted (see, e.g., Palla & Stahler 1999). The square outline in this figure indicates the restricted range of parameter space plotted in Figures 9a–9d, in order to emphasize the improved precision with which the different sets of tracks can be compared using the WL 20 data.

The two sources of systematic error in our luminosity determinations are the adopted distance, for which we are using the *Hipparcos*-determined value, and the adopted $A_V = 16.3$. An error in the distance will move both sources up by the same amount in each panel of Figure 9: a distance of 140 pc will raise the points by ~ 0.06 units in the logarithm, or about one small tick mark along the luminosity axis. Similarly, a slightly greater value of extinction than the value of $A_V = 16.3$ adopted here will also move the position of each source up vertically in Figure 9. With an extreme value of $A_V = 18$, the luminosities are increased by $\sim 33\%$; 0.12 in the logarithm, or 2.5 small tick marks.

From spatially resolved near-IR spectroscopy, Luhman & Rieke (1999) determine the spectrum of WL 20 W to be consistent with a photosphere of spectral type M2–K6, corresponding to a temperature range $3513 \text{ K} \leq T_{\text{eff}} \leq 4205 \text{ K}$, with an adopted spectral type of M0 (corresponding to $T_{\text{eff}} = 3850 \text{ K}$). The same authors assign a K6 ($T_{\text{eff}} = 4205 \text{ K}$) spectral type to WL 20 E, with possible spectral types in the range K5–K7, corresponding to $4060 \text{ K} \leq T_{\text{eff}} \leq 4350 \text{ K}$. In Figure 9, we indicate the possible effective temperature range for each source by the horizontal error bars.

Inspection of Figure 9 shows that none of the models rule out WL 20 E and W being a coeval pair, within the allowable errors in spectral type for each source. However, the derived ages and masses differ among the models. The D’Antona & Mazzitelli (1998) tracks yield a system age of $\sim (2.0\text{--}2.5) \times 10^6 \text{ yr}$, with a mass of 0.62–0.68 M_{\odot} for WL 20 E and a mass of 0.51–0.55 M_{\odot} for WL 20 W. All the other models yield a system age twice as old: $(4\text{--}5) \times 10^6 \text{ yr}$. For an age of $4 \times 10^6 \text{ yr}$, the Baraffe et al. (1998) models yield masses of 0.86 and 0.68 M_{\odot} for WL 20 E and W, respectively. The Palla & Stahler (1999) tracks yield a coeval system age of $5 \times 10^6 \text{ yr}$, with masses of 0.83 M_{\odot} for WL 20 E and 0.70 M_{\odot} for WL 20 W. Similarly, the Siess et al. (2000) tracks yield a coeval system age of $5 \times 10^6 \text{ yr}$, with masses of 0.85 M_{\odot} for WL 20 E and $\sim 0.65 M_{\odot}$ for WL 20 W.

Of the two possible ages for this system, $(4\text{--}5) \times 10^6$ and $(2.0\text{--}2.5) \times 10^6 \text{ yr}$, the younger age is the more plausible, especially when we consider that WL 20 S, which appears to be a Class I object, is also part of this system. Based on statistical arguments, Class I objects are generally thought to be just a few times 10^5 yr old (Wilking et al. 1989), maybe $8 \times 10^5 \text{ yr}$ at most (Kenyon et al. 1990). Previous statistical studies have ignored the systematic effects introduced by unresolved binary/multiple systems, however, which have the effect of making a source appear brighter (and, therefore, judged to be younger) than is in fact the case. Such an effect can result in derived ages of a factor of 2 too young (White 1999), so that the oldest Class I sources may be of order $1.6 \times 10^6 \text{ yr}$ old, just about consistent with the $(2.0\text{--}2.5) \times 10^6 \text{ yr}$ system age derived from the D’Antona & Mazzitelli (1998) tracks.

Very recently, PMS tracks that include the effects of accretion on the models have been calculated by Tout, Livio, & Bonnell (1999). These authors provide the magnitude of the errors possible when one derives ages and masses of PMS objects from evolutionary tracks that ignore accretion, such as the ones discussed above. In particular, placement of WL 20 E and W on their Figure 14 shows that the derived age from the other tracks, including those of D’Antona & Mazzitelli (1997), can be up to a factor of 2 too old relative to accreting PMS models, making the true ages of WL 20 E and W as young as $(1\text{--}1.3) \times 10^6 \text{ yr}$, consistent with the oldest plausible Class I source age of $1.6 \times 10^6 \text{ yr}$ for WL 20 S. The errors in the masses of PMS objects derived from nonaccreting versus accreting tracks are much smaller, being negligible in the case of WL 20 E and at the 10% level for WL 20 W (found by placing these sources on Fig. 13 of Tout et al. 1999).

4.3. Nature of WL 20 S

In this work, we have found that (1) WL 20 S is the reddest and most luminous member of the WL 20 system, (2) it is highly variable on timescales of a few years, (3) it

⁴ As updated in 1998 at <http://www.mporzio.astro.it/~dantona/prems.html>.

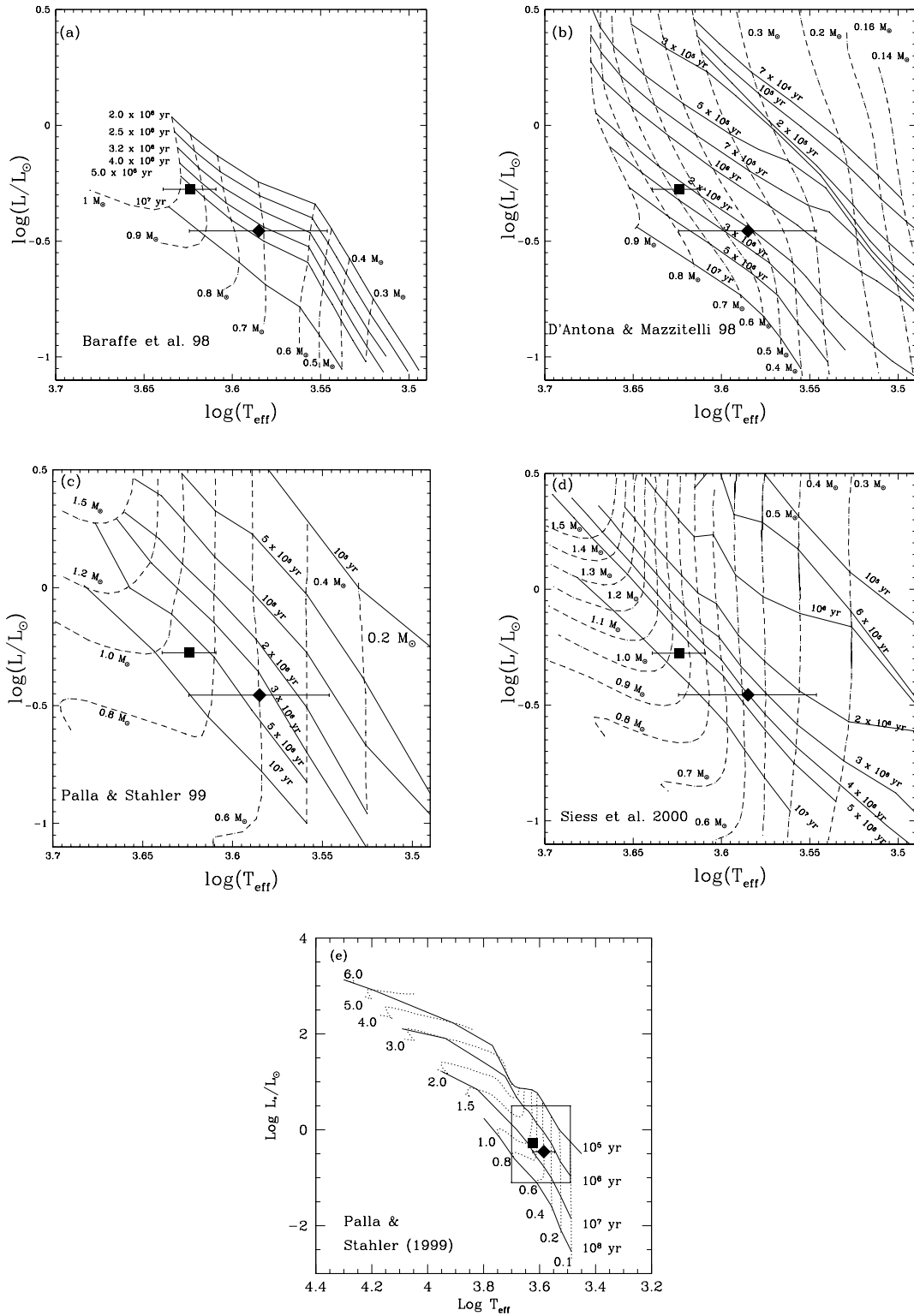


FIG. 9.—Testing pre-main-sequence evolutionary tracks with the WL 20 system: (a)–(d) display four separate sets of PMS evolutionary tracks over magnified luminosity and temperature ranges. The stringency with which we are testing and comparing these models is illustrated by the outlined box in (e), which indicates the parameter ranges of the plots presented in (a) compared with the scale of previously plotted PMS tracks (e.g., Palla & Stahler 1999). In all the panels, solid lines indicate isochrones, dashed lines indicate isomass tracks, the square represents WL 20 E, and the triangle represents WL 20 W. (a) Baraffe et al. (1998) tracks. The youngest coeval system age still within the errors is 4×10^6 yr. (b) D’Antona & Mazzitelli (1998) tracks. The adopted temperatures and luminosities of WL 20 E and W are consistent with an age of $(2.0\text{--}2.5) \times 10^6$ yr. This is the most plausible (youngest) system age given by any of the tracks presented here, as discussed in the text. (c) Palla & Stahler (1999) tracks. The youngest system age, still within the data errors, and subject to the coevality constraint is $\sim 5 \times 10^6$ yr. (d) Siess et al. (2000) tracks. The youngest system age still within the data errors subject to the coevality constraint $\sim 5 \times 10^6$ yr. (e) The usual scale to which PMS tracks are plotted. The rectangular area outlines the plot limits of (a)–(d), to highlight the refined time resolution at which these tracks are tested by the WL 20 system.

contains most of the dust in the system in a mid-IR-emitting region some 40 AU in diameter, and (4) it is the source of the observed centimeter emission.

The most likely explanation for the mid-IR appearance of WL 20 S is that it is experiencing a phase of enhanced (and varying) accretion activity, perhaps due to interactions with its neighbors. This is especially likely in view of the fact that the SED of WL 20 S is consistent with the presence of a flared disk of ~ 250 AU in radius (Chiang & Goldreich 1999, eq. [1]), very similar to the projected separation of 280 AU between WL 20 S and W. We observe a structure whose 40 AU diameter size appears to be wavelength independent in the mid-IR: this structure may be the flared disk surface. The *IRAS* fluxes for the WL 20 system, as a whole, are systematically larger than the sum of the fluxes of the individual components derived from ground-based observations (see Table 2). This discrepancy in the measured fluxes in different-sized beams implies the presence of material on scales larger than those to which the ground-based observations are sensitive, but that still fall within an *IRAS* beam. Thus, $\geq 40\%$ of the observed *IRAS* fluxes are emitted from regions $10''$ – $120''$ in size, corresponding to the size scales of infalling envelopes. It may very well be that WL 20 S is actively accreting matter from the envelope, through its flaring disk, while its companions have already ceased significant accretion.

If this is true, it addresses one of the primary objections to WL 20's being a true triple system, as opposed to a chance superposition of a binary (WL 20 E and W) with a single source (WL 20 S). If WL 20 is a triple with an age of $\sim 2 \times 10^6$ yr, that is still uncomfortably old to have the presence of a Class I source, which would normally be presumed to be less than 1×10^6 yr old. This would appear to argue that WL 20 S is more likely a chance superposition. However, if accretion has been continued to a late phase because of tidal interactions with the other members, then the shape of the SED of an individual source within a binary/multiple system is an indicator only of the accretion activity of that source and has little to do with its age.

Preliminary studies of accretion in triple systems have so far focused on hierarchical triples, in which the separation between two sources is much smaller than their distance to the third component, a circumstance clearly not applicable to the WL 20 system. In fact, if formation proceeds through fragmentation, then the resultant triples are typically not in a very hierarchical configuration. The stability of accreting triples has been examined by Smith, Bonnell, & Bate (1997). In general, if the maximum separation of the closer pair (280 AU projected separation for WL 20 S and W) is comparable to the minimum separation of this pair to the third component (400 AU projected separation from WL 20 W to E), then the stability of the system is questionable. From the above analysis of existing PMS models, the current best mass determinations for this system are 0.62 – $0.68 M_{\odot}$ for WL 20 E and 0.51 – $0.55 M_{\odot}$ for WL 20 W, and $\sim 1.0 M_{\odot}$ for WL 20 S from the constraints given by its 1.0 – $1.8 L_{\odot}$ luminosity. According to the criterion for stability of triple systems given by Harrington (1977), as quoted by Smith et al. (1997), the WL 20 system should be dynamically unstable. The behavior of dynamically unstable accreting triple systems has not yet been examined. It may be that some fraction of single stars are formed from the disintegration of unstable triple systems.

5. CONCLUSIONS

We have presented subarcsecond, mid-infrared imaging photometry of the WL 20 triple system at 7.9, 10.3, 12.5, 17.9, 20.8, and $24.5 \mu\text{m}$. When supplemented with spatially resolved, near-infrared imaging photometry from ProtocAM at the IRTF, these combined data allow solid determinations of the spectral energy distribution of each source individually, as well as accurate luminosity determinations. We find the source luminosities for WL 20 E, W, and S to be 0.61, 0.39, and 1.0 – $1.8 L_{\odot}$, respectively. For WL 20 E and W, 0.53 and $0.35 L_{\odot}$ can be attributed to photospheric emission alone.

WL 20 can now be classified as an “infrared companion system,” with WL 20 S exhibiting an embedded protostellar (Class I) SED, while its two neighbors, WL 20 E and W, each exhibit a T Tauri star (Class II) SED. The infrared companion, WL 20 S, is the dominant luminosity source in the system. WL 20 S differs from its T Tauri companions in three important respects: (1) its near- and mid-IR fluxes vary significantly over timescales of years; (2) it is well resolved at mid-IR wavelengths, with a constant, wavelength-independent source diameter of 40 AU; and (3) it is found to be the source of the radio centimeter emission in the system.

Since the effective temperatures of WL 20 E and W are known from spatially resolved near-IR spectroscopy, we can place these sources on an H-R diagram. We are thus able to test currently available pre-main-sequence evolutionary tracks at unprecedentedly high temporal resolution, and we find that of the nonaccreting models, the D'Antona & Mazzitelli (1997) tracks yield the most plausible system age, at $(2.0$ – $2.5) \times 10^6$ yr. The inferred source masses from these tracks at these ages are 0.62 – $0.68 M_{\odot}$ for WL 20 E and 0.51 – $0.55 M_{\odot}$ for WL 20 W.

We cannot, at present, independently determine a mass or age for the infrared companion, WL 20 S. However, the intriguing possibility now exists of determining the spectral type and, therefore, the effective temperature of this embedded source with the new generation of high-resolution spectrographs on 8–10 m ground-based telescopes. Once an effective temperature determination has been made spectroscopically, and assuming system coevality, one could locate WL 20 S on an isomass track, independently of its known luminosity. Thus, the possibility exists, for the first time, to directly derive the accretion luminosity of a Class I protostar.

Millimeter interferometry of this unique triple system would advance our understanding of the gas dynamics involved, processes that cannot be explored in any other way. Higher temporal resolution, spatially resolved imaging and monitoring of WL 20 at infrared wavelengths, combined with detailed modeling of its appearance, will also lead to a more detailed understanding of the actual accretion processes taking place in WL 20 S.

We wish to thank Michael Werner for a critical reading of this manuscript, and Bruce Wilking and Tom Greene for useful discussions and for providing the impetus to publish these results. The anonymous referee provided a number of comments, particularly in regard to the luminosity calculations, for which we are grateful. We also thank Bruce Wilking, Derek Ward-Thompson, and Jason Kirk for providing us with data in advance of publication, and Russel White for providing computer-readable versions

of certain sets of PMS tracks. M. E. R. thanks Fred Chaffee and the entire Keck Observatory staff for their enthusiasm, patience, and assistance in making it possible to use MIRLIN on the Keck II Telescope. The staffs of the Palomar Observatory and the NASA IRTF have also continued to provide outstanding support for MIRLIN as a visitor instrument on their respective telescopes. Portions of this work were carried out at the Jet Propulsion Laboratory, California Institute of Technology, under contract

with the National Aeronautics and Space Administration. Development of MIRLIN was supported by the JPL Director's Discretionary Fund, and its continued operation is funded by a Supporting Research and Technology award from NASA's Office of Space Science. M. B. gratefully acknowledges support from the National Science Foundation through grants AST 97-31797 and AST 00-96087 to Harvey Mudd College, which have made her contributions to this work possible.

REFERENCES

- Adams, F. C., Lada, C. J., & Shu, F. H. 1987, *ApJ*, 312, 788
 André, P., & Montmerle, T. 1994, *ApJ*, 420, 837
 Baraffe, I., Chabrier, G., Allard, F., & Hauschildt, P. H. 1998, *A&A*, 337, 403
 Barsony, M., Burton, M. G., Russell, A. P. G., Carlstrom, J. E., & Garden R. 1989, *ApJ*, 346, L93
 Barsony, M., Kenyon, S. J., Lada, E. A., & Teuben, P. J. 1997, *ApJS*, 112, 109
 Barsony, M., Ressler, M. E., & Casement, S. 2001, in preparation
 Bate, M. R., & Bonnell, I. A. 1997, *MNRAS*, 285, 33
 Beck, T. L., Simon, M., Ghez, A. M., Prato, L., & Howell, R. R. 2000, *BAAS*, 196, 407
 Beichman, C. A., Neugebauer, G., Habing, H. J., Clegg, P. E., & Chester, T. J. 1988, *IRAS Catalogs and Atlases Explanatory Supplement* (NASA RP-1190) (Washington: GPO)
 Chiang, E. I., & Goldreich, P. 1999, *ApJ*, 519, 279
 D'Antona, F., & Mazzitelli, I. 1998, *Pre-Main-sequence Tracks and Isochrones*, (updated 1998; Rome: Astron. Obs.)
 de Geus, E. 1992, *A&A*, 262, 258
 de Geus, E., de Zeeuw, P., & Lub, J. 1989, *A&A*, 216, 44
 de Zeeuw, P. T., Hoogerwerf, R., de Bruijne, J. H. J., Brown, A. G. A., & Blaauw, A. 1999, *AJ*, 117, 354
 Draine, B. T., & Lee, H. M. 1984, *ApJ*, 285, 89
 Ghez, A. M., Neugebauer, G., Gorham, P. W., Haniff, C. A., Kulkarni, S. R., Matthews, K., Koresko, C., & Beckwith, S. 1991, *AJ*, 102, 2066
 Gorham, P. W., Ghez, A. M., Haniff, C. A., Kulkarni, S. R., Matthews, K., & Neugebauer, G. 1992, *AJ*, 103, 953
 Greene, T. P., & Lada, C. J. 1996, *AJ*, 112, 2184
 Greene, T. P., & Meyer, M. R. 1995, *ApJ*, 450, 233
 Harrington, R. S. 1977, *AJ*, 82, 753
 Kenyon, S. J., Hartmann, L. W., Strom, K. M., & Strom, S. E. 1990, *AJ*, 99, 869
 Kenyon, S. J., Lada, E. A., & Barsony, M. 1998, *AJ*, 115, 252
 Knude, J., & Høg, E. 1998, *A&A*, 338, 897
 Lada, C. J. 1987, in *Star Forming Regions*, ed. M. Peimbert & J. Jugaku (Dordrecht: Reidel), 1
 Lada, C. J., & Wilking, B. A. 1984, *ApJ*, 287, 610
 Leous, J. A., Feigelson, E. D., André, P., & Montmerle, T. 1991, *ApJ*, 379, 683
 Luhman, K. L., & Rieke, G. H. 1999, *ApJ*, 525, 440
 Mathieu, R. D. 1994, *ARA&A*, 32, 465
 Palla, F., & Stahler, S. W. 1999, *ApJ*, 525, 772
 Rieke, G. H., Ashok, N. M., & Boyle, R. P. 1989, *ApJ*, 339, L71
 Siess, L., Dufour, E., & Forestini, M. 2000, *A&A*, 358, 593
 Smith, K. W., Bonnell, I. A., & Bate, M. R. 1997, *MNRAS*, 288, 1041
 Strom, K. M., Kepner, J., & Strom, S. E. 1995, *ApJ*, 438, 813 (SKS)
 Tout, C. A., Livio, M., & Bonnell, I. A. 1999, *MNRAS*, 310, 360
 Ward-Thompson, D., & Kirk, J. 2001, in preparation
 White, R. 1999, Ph.D. thesis, UCLA
 Whittet, D. C. B. 1974, *MNRAS*, 168, 371
 Wilking, B. A., & Lada, C. J. 1983, *ApJ*, 274, 698
 Wilking, B. A., Lada, C. J., & Young, E. T. 1989, *ApJ*, 340, 823
 Wilking, B., Bontemps, S., Schuler, R., Greene, T., & André, P. 2001, *ApJ*, in press
 Young, E. T., Lada, C. J., & Wilking, B. A. 1986, *ApJ*, 304, L45 (YLW)